The Value of Information from Horizontal Distributed Acoustic Sensing Compared to Multicomponent Geophones via Machine Learning

Samir F. Jreij, Whitney J. Trainor-Guitton, Michael Morphew, Ivan Lim Chen Ning

July 23, 2020

Abstract

Faults play an important role in recharging many geothermal reservoirs, and seismic information can image the locations of these faults. The value of information (VOI) metric is used to objectively quantify and compare the value of two types of seismic receiver data via a machine learning approach. The demonstrated VOI methodology is novel by including spatial models from seismic data and obtaining the information statistics from machine learning. Our 2D numerical experiments compare images created from sparsely-spaced (80m), two-component geophone sampling to high spatial resolution (1 m), single-component DAS. We used a 3-fold cross validation of a U-Net CNN to achieve average classification statistics. The results suggest that when horizontal sources are utilized, geophones and DAS identify reflectors and non-reflectors at roughly the same rate. The average F1 score for horizontal DAS is 0.939 and 0.931 for geophones. For images created from a vertical source, DAS performed marginally better (F1=0.919) than geophones (F1=0.877). Our transferrable methodology can provide guidance on which acquisition scenarios can improve images of important structures in the subsurface, and presents an efficient method for obtaining reliability statistics from high dimensional, spatial data.

1 Introduction

Drilling decisions for geothermal development are full of uncertainty. Designing a data collection regime is not easy given the high degree of complexity found in the heterogenous subsurface. Likewise, there is always uncertainty associated with different data types' ability resolve the magnitude of permeability and temperature or the presence of fluids, all of which ultimately determine a geothermal reservoir's capacity. Value of Information (VOI) theory provides a powerful framework for determining the utility of information when making decisions with uncertain outcomes [1]. The VOI metric has the potential to be extremely useful for subsurface characterization, as new data collection is often expensive and its efficacy is uncertain.

Historically, non-dimensional probability distribution functions are used to describe the "imperfectness" of geophysical attributes to correlate with rock properties [2; 3]. [4] introduced spatial correlation of porosity via 2D reservoir models to demonstrate the value of combined CSEM and seismic amplitude measurements via VOI. [5] provides an overview of VOI for oil and gas decisions, noting that up to its publishing date most reliability assessments of the information relied on subjective expert opinion, where the reliability is the quantitative measure of the "imperfectness" of the information source being evaluated. [6; 7; 8] are examples of assessing geophysical data worth for aquifer management. VOI evaluations have also been developed for geothermal exploration focusing on how inversion of magnetotelluric data affects the spatial interpretation of clay cap locations or thickness [9; 10].

None of the previous VOI work utilized spatial models built by seismic data. Active seismic surveys can provide more reliable 3D and 4D measurement of the subsurface, compared to other diffusive geophysical measurements. This paper is motivated by the active seismic source experiments from the PoroTomo project (short for Poroelastic Tomography by Adjoint Inverse Modeling of Data from Seismology, Geodesy, and Hydrology) In March 2016, PoroTomo acquired four-weeks of geodesy, interferometric synthetic aperture radar (InSAR), hydrology, distributed temperature sensing, passive source seismology, and active source seismology data [11; 12]. These data were jointly collected to characterize rock mechanical properties and faults, which provide permeability for geothermal fluid movement, of Brady Natural Laboratory, an 18 MegaWatt-producing geothermal field. Faults are a potential seismic target as they may represent geologic offsets and thus provide seismic reflections, both of which have been previously interpreted from seismic data at Brady [13; 14]. The survey included 238 multi-component geophones, 156 three-component (vertical and orthogonal horizontal) vibroseis source locations that swept from 5 to 80 Hz in 20 seconds, 300 meters of borehole (vertical) and nearly nine kilometers of trenched, surface (horizontal) fiber-optic cable.

In this paper, we use migration to evaluate how well the faults at Brady could be located using the receiver information from the horizontal DAS and two-component (2C) geophones. Seismic migration models are used to construct 3D subsurface features by simulating the source and receiver wavefields [15]. Different prestack depth migration experiments are implemented, inspired by the acquisition geometry of PoroTomo and *a priori* fault information of Brady.

Figure 1 displays the PoroTomo survey geometry of the vibroseis locations, the geophones and the horizontal fiber optics, which recorded both distributed acoustic and temperature sensing (DAS and DTS) data. The geophones have an average inline spacing of 80 meters. This spacing is considered sparse for active-seismic applications, which generally will have an average geophone spacing closer to 20 meters, and was due in part to permitting issues around existing historical sites in the area [16].

To demonstrate our VOI methodology, we use the PoroTomo field acquisition parameters to generate synthetic DAS and geophone data. We use synthetic data for two main reasons: 1) the ability to produce many, "ground truth" training models for statistical learning and 2) issues with the real PoroTomo active source dataset. For the statistical learning, we use convolutional neural networks (CNN) to provide classification accuracies to compare between migration models constructed by horizontal DAS versus 2C geophones [17; 18]. Although vertical DAS field data from the active source surveys were useful for migration [14], and the passive horizontal DAS field data were successful in detecting regional earthquakes [19; 20], unfortunately, the sparse geophones and short offset of the survey (max 1,100m, see Figure 1) created spatial aliasing and lack of moveout observed in the PoroTomo data, respectively. Noise removal thus was extremely challenging and extended beyond the capability of the original team and available resources.

The objective of this paper is to present a novel VOI methodology that uses a CNN algorithm to statistically compare spatial models (2D images) from two types of seismic data. We present 2D numerical experiments to demonstrate how our methodology captures physical strengths and weaknesses of the multi-component geophones and the spatially-dense DAS data, both alone and together. This is assessed through the 183 2D reflectivity models constructed from reverse time migration of the data. As we will describe, our synthetic simulations cannot capture all of the challenges that will encumber seismic data, especially DAS. We emphasize that the current DAS and geophone comparison are an illustration of a methodology. This methodology is transferable to other scenarios beyond the experiments presented in the paper; it can provide guidance on other data types that produce spatial images of important structures in the subsurface.

The paper is organized as follows. Section 2.1 describes the posterior probability statistic needed for VOI

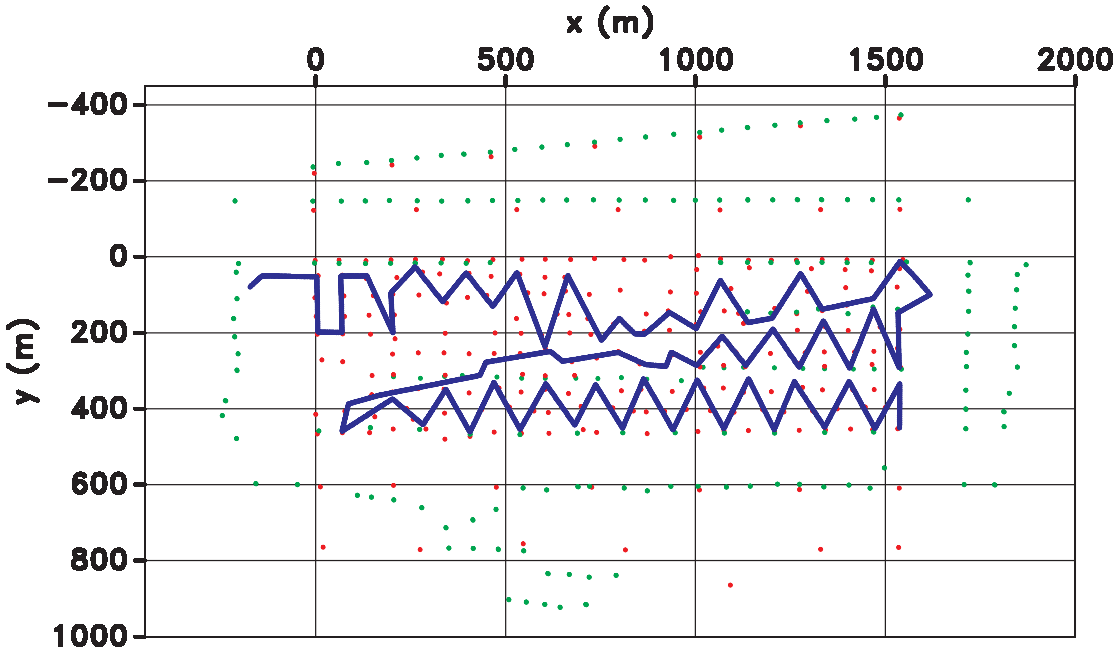

Figure 1: PoroTomo survey geometry. Green dots represent source locations, red dots represent geophone locations, and the blue line represents the surface DAS layout.

calculations and the fault model of Brady Hot Springs that serve as the decision variable and labels. Section 2.2 describes modeling that simulates the DAS and geophone measurements. This section also describes the migration method used to reconstruct the fault locations from these seismic measurements, which are used as the ”features” in machine learning. Section 2.3 describes how the CNN U-Net algorithm is trained separately on the different migrations models from the DAS, geophone and the different source scenarios. Finally, Section 3 presents the posteriors and VOI for the different receiver and source combinations.

2 Methodology

This section describes our methodology that quantifies the accuracy of fault locations in the 2D subsurface. First, we describe the value of information metric and the fault model used. Next, we briefly introduce the imaging approach, which accounts for the different sensitivities and spatial densities of the two sensors: 2C geophone and horizontal fiber. Lastly, the efficient and novel method for assessing the reliability of the images obtained from different sensors via convolutional neural networks (CNN) is described.

2.1 Value of Information (VOI)

The VOI method accounts for the uncertainty of a particular information source through the posterior distribution,

$$Pr(\Theta = \theta_i|\Theta^{int} = \theta_j)_{S,R} = \frac{(Pr(\Theta = \theta_i))Pr(\Theta^{int} = \theta_j|\Theta = \theta_i)}{Pr(\Theta^{int} = \theta_j)}; \forall i, j = F, NF \tag{1}$$

where θ can represent the actual occurrence of a structure in the subsurface and θ^{int} represents the interpreted structure from the proposed (geophysical) data. For the purposes of our VOI problem definition,

the fault locations are the decision variable θ. Specifically for the PoroTomo example, the reliability will quantify how often interpretations of faults ($\theta^{int}_{j=F}$) align with the actual presence of faults ($\theta_{i=F}$), and vice versa. Faults are important structures for geothermal systems: they often provide fluid conduits for both upward and downward circulation, allowing for production and recharge of geothermal fluids [21]. Therefore, at each location within a migrated image, there would be either a fault (*F*) or absence of a fault (*NF*). The reliability is a conditional or posterior probability, which summarizes how frequently the interpretations from geophysical information align correctly or incorrectly with actuality and can be thought of as capturing the "imperfectness" of the information being considered. Lastly, the subscript S and R represent the types of source and receivers used to obtain the information. As described in the next section, we have six combinations of different S and R, two sources $S = (horizontal, vertical)$ and three receivers $R = (geophones, DAS, both)$. Therefore, all combinations of S and R result in six possible posteriors (Equation 1).

The value with imperfect information

$$V_{imperfect\ S,R} = \sum_{j=F,NF} Pr(\Theta^{int} = \theta_j) \max_a \left[\sum_{i=F,NF} Pr(\Theta = \theta_i | \Theta^{int} = \theta_j)_{S,R}\ v_a(\theta_i) \right] \tag{2}$$

uses the posterior (Equation 1) as a weight on utility outcomes (v) from different decision alternatives (a, e.g. drill or don't drill), as represented by $v_a(\theta_i)$ [9]. To quantify and compare the value of using distributed acoustic sensing versus geophones in surface acquisitions, six reliabilities (Equation 1) can be calculated to get six $V_{imperfect}$'s: geophone, DAS and the combination of both (3 R's) with both a horizontal and a vertical source (2 S's). The focus of our work is to quantify the "imperfectness" or the posterior probability for seismic images created with the different sensors R; in the Results section (Section 3), we will use nominal utility outcomes (v) and simple possible alternatives (a), to demonstrate final $V_{imperfect}$ values.

2.1.1 2D Fault / Not Faults Models: Decision variable & Labels for CNN-UNet

For all six reliabilities computed, the faults shown in Figure 2 serve as the true fault locations: $\theta_{i=F}$. These are the *a priori* locations of major faults given legacy seismic and well observations as interpreted by [22]. Some of the faults are interpreted to have up to 10 meters of displacement and thus could provide reflections of the seismic energy [13]. Therefore, the faults both serve as a subsurface structure that will influence geothermal production decisions (e.g. ideal locations for new wells) and as a subsurface feature that can be mapped by reverse-time migration of geophone and/or DAS data (described in the next section).

To compare images from the geophones, DAS and a combination of the two, 183 2D slices are taken from the 3D model (Figure 2a) along the main faults' strikes (the PoroTomo y-axis). One example slice, which contains a variety of structural dips, is shown in Figure 2b. The faults are used as a reflectors within a constant velocity model.

Figure 3 demonstrates the Methodology workflow. This Section (Section 2.1) covered the fault model and its importance to geothermal decision-making, which is captured in the VOI metric. The next section (Section 2.2) will describe the sources, receivers and migration technique which creates the 2D seismic images. Section 2.3 will describe how six CNN models, one for each source and receiver combination, will be trained and tested to obtain the reliability statistics (Eqn 1). The labels (fault/not fault) come from our best understanding of Bradys geothermal reservoir (Figure 2) and the migration images of Section 2.2 serve as the "features" for the CNN U-net model.

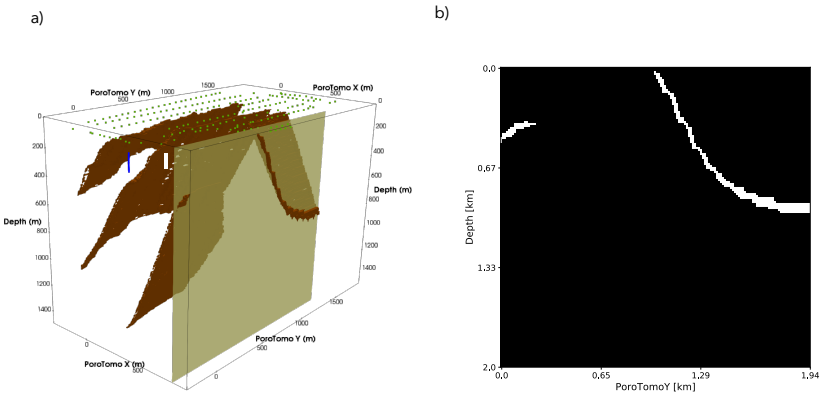

Figure 2: **a**) *a priori* fault model from [22] with source locations in green on the surface. **b**) One example 2D cross section from the 3D model in *a*, represented by150x155 pixels. The faults (in white) serve as reflectivity boundary for seismic exploration.

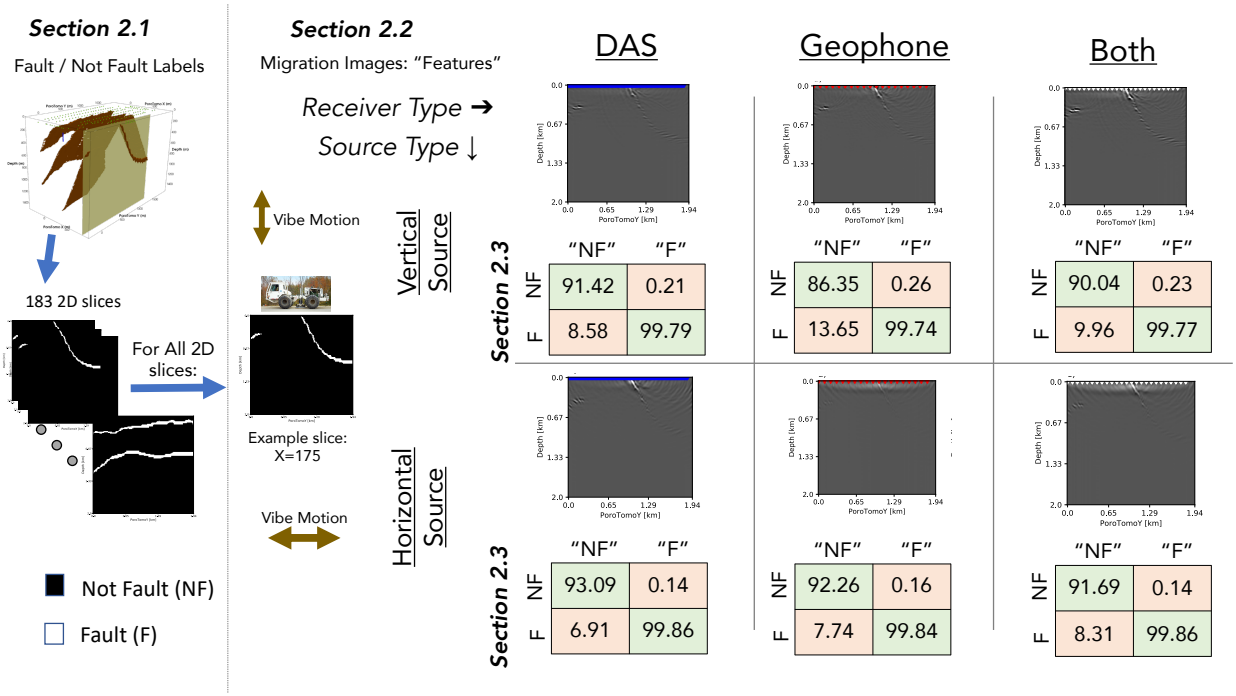

Figure 3: Workflow for 2D fault images and their respective statistics. Section 2.1 Fault model: the decision parameter = seismic reflectors = labels in machine learning. Section 2.2 Seismic images: imperfect information about the fault locations (2D "features"). Rows= sources type. Columns= receiver type. Section 2.3: Posterior statistics from CNN.

2.2 Spatial Models with Migration: Computing the Features for CNN UNet

This subsection describes how spatial models from the seismic data are constructed to assess if a fault exists or not at a certain location. Importantly, the imperfectness of the sensors will depend on the physical limitations of the sensors to create accurate prestack depth images. Reverse time migration (RTM) is used for the experiments to convert the synthetic seismic data into information about the fault positions in the subsurface. First, we describe how we model the measurement for each sensor type separately.

2D elastic forward modeling is used to produce strain (as measured by DAS) and displacement (as measured by geophones) data along the surface of our 2D example excited by both horizontal and vertical forces separately. DAS strain measurements, aligned in the X-plane ε_{XX}, are measured every one meter across the experiment surface and integrated over a gauge length (described further below). Vertical and horizontal particle displacement (u_z and u_x, e.g. two components) represent the geophone measurements and are recorded every 100 meters. As seen in Figure 1, the PoroTomo survey did not include a straight fiber that was this long. It did include, however, a maximum offset of 1,500-meters across the entire survey. A 2D line of 1,500 meters was utilized to numerically simulate data with similar offsets as the PoroTomo survey.

Unlike the geophones, which are a point-sensor, DAS is a "linear" sensor: averaging the distributed measurements (e.g. strain or more precisely differential displacement over a gauge length) along the fiber. Thus, an attribute that needs to be modeled is the gauge-length. The gauge-length of fiber acts as a moving average [23]. The gauge-length in the PoroTomo survey was set at 10-meters, so the modeled data is a matrix multiplication of $\frac{1}{10}$ for the gauge length, the spatial sampling 1-meter, and the raw point strain data simulated by the finite difference code after [24] which utilizes the Madagascar software package [25].

To produce images from the simulated seismic measurements, we use reverse time migration (RTM). In simple terms, reverse-time migration, pioneered by [15], is a technique that numerically simulates both the source wavefield W_S (produced by the seismic vibrator) and the recorded wavefield signal W_R (recorded by the sensor, either the DAS or geophones) with the objective of constructing 2D or 3D models that locate where prominent reflectors are in the subsurface. W_S is propagated forward in time, and the observed or synthetic data, W_R, are backward-propagated in time in the same space. Both wavefields are then cross-correlated at each time step t, and summed across all time steps to form the final image R as follows:

$$R(x) = \sum_{k,t} W_S(k, x, t) W_R(k, x, t) \tag{3}$$

where x is a vector of spatial coordinates and k the shot index. By computing the cross-correlation of the two wavefields, RTM attempts to locate where reflectors are in the 3D subsurface. This zero-lag cross-correlation is known as the imaging condition. The energy-norm imaging-condition is used to combine the source and receiver wavefields [26]. In this work, the energy-norm creates a single elastic image that represents the measure of reflected energy; importantly for this work, it produces one final image that allows for an easy comparison of migrated elastic data between geophone and DAS data.

Two-dimensional elastic forward modeling is used to produce two types of W_R: strain (as measured by DAS) and particle velocity (as measured by geophones). Both receiver wavefields are recorded along the surface for our experiments. Two different sources are required to create the receiver wavefield W_R, which will be back-propagated. An acceleration force is used for back propagation of the geophone data and a stress tensor is used for back propagation of the DAS data. Next, the source wavefield W_S is generated. The source wavefield is a forward modeled from the original source locations through a smooth velocity model.

Ideally, to generate the combined image (DAS with geophones) the back-propagation of the two data types (ε and u) should be done simultaneously, but this was not possible with current codes, so the data are back propagated individually. The geophone and DAS reflectivity are normalized separately and then added together to create the combined image. We recognize that normalizing and adding together is not the ideal method to combine the two images from the different data types. However, we contend that our goal was to construct the entire VOI workflow, thus the improvement on combining the images can be future work. Our objective of assessing the non-ideal combination image was to see if artifacts from the separate images would be cancelled out.

The broadside insensitivity of DAS describes its inability to record signals which arrive perpendicular the the DAS cable [27]. Optical fiber recording is a widely accepted for downhole VSP recording [28; 29; 30; 31; 32; 33]; the strong reflected, primary-wave signal will intercept the vertical well parallel to the fiber, providing the highest recording sensitivity for DAS. In a borehole, the vertical fiber is insensitive to the horizontal component of strain, ε_{XX}; however for surface (horizontal) DAS, this is the component that is measured. [32] and [34] represent the published studies with active-source, surface (horizontal) DAS acquisitions. Daley et al. [32] experiment with a vertical vibrator (vertical-force) source. The authors concluded that the offset-to-reflector depth ratio was not sufficient to record the reflected P-wave on the DAS fiber due to the relatively small incidental reflected angle and low signal-to-noise ratio. Horizontal source mechanisms must be investigated before such a conclusion can be made about the feasibility of using surface DAS fiber.

For our 2D experiments, both vertical and horizontal force sources are modeled to represent a vertical and horizontal vibe sources, which were also collected for the PoroTomo field experiment [11]. Surface DAS data will have directional sensitivity to different types of waves. Since surface horizontal DAS is sensitive to the horizontal component of particle differential displacement, short-offset P-wave reflections will not be recorded on surface DAS, assuming a flat-layered earth. This is not the case for our experiments which are modeled after the steeply dipping faults at Brady (see Figure 2).

Seismic sources in the PoroTomo experiment are not on a uniform grid, and the source spacing is as large as 150 meters. A constant source spacing of 75 meters (which is about the average source spacing in the PoroTomo survey) is used to minimize migration artifacts from poor illumination. Seismic illumination describes how well the 3D subsurface is sampled and is determined by the source-receiver geometry and velocity model [35]. The velocity model used was generated from observed Brady data and is described in both [36] and [14].

2.3 Efficient reliability statistics via Convolutional Neural Network Analysis

This paper presents the first demonstration of VOI applied to seismic migration images; thus, the fault/no-fault interpretations, θ^{int}, derive from these images. The interpretations are achieved efficiently via a machine learning approach to interpret the respective fault and no-fault features in the migrated image, providing a measure of the "imperfectness" of the seismic image, described by Equation 1. Next, we describe how convolutional neural networks (CNN) are applied to detect faults within the seismic image, and return the Bayesian statistics needed for a VOI evaluation. The common application of CNN's to images is to predict labels from features. In a slight contrast to the mainstream application, the role of the CNN for our study is to compare the quality of the images across the six source and receiver combinations; we do this by separately training the CNN on each combination.

Neural networks are one of the most powerful machine learning algorithms that can be utilized for object recognition in the seismic images. Convolutional Neural Networks (CNN) in particular are at the core of most state-of-the-art computer vision solutions [17]. In particular, our goal is a semantic segmentation, in which the machine learning algorithm classifies every pixel in our model as fault or not-fault. U-net is a CNN originally used for biomedical image segmentation, but it is also applicable to geophysics image segmentation due to the similarities between the problems of identifying cell divisions and identifying faults [18].

U-net functions much like a typical CNN, but it utilizes additional operations that create the "U" shape architecture shown in [18]. The seismic migration images along with their labels are inputted at the top left of the "U" network. The images are then re-sampled, cropped or re-scaled as they travel down and across the "U", through various layers of convolutional filters, cropping, and pooling functions. The physical distance represented by the space between two pixels increases as the U-net progress downward, allowing the U-net to capture features at different scales. The U-net then expands upward on the right-hand portion of the "U" network as the image is scaled back upward so that pixel-wise segmentation can be performed. The output at the top right of the "U" are N probability maps, where N is the number of classes being segmented by the neural network. In our case there are two probabilities associated with either a fault or not fault occurring.

After two convolutional layers, the seismic image is downsampled through a max-pooling operation, in which the highest value in a sliding 2x2 filter is taken as the representative value for that window (red vertical arrows). This pattern continues for several cycles until the bottom of the U-net is reached. The seismic images are then upsampled after every two convolutional layers via a transposed convolution, otherwise known as deconvolution [37]. The final layer is a 1x1 convolution that assigns a set of probabilities (ranging from 0 to 1) for each pixel that represent how certain that the pixel belongs to each class.

Throughout the network, the feature maps are periodically copied and sent to the other side of the "U". This process serves a couple of purposes. First, it enforces regularization upon the network, preventing the U-net from becoming too focused on a single representation of a fault. The copy layers also help with back-propagating weight updates for the convolutional filters through the network during learning, as weight updates can reach the earliest layers more quickly than without the copy layers.

Besides the copy layers, the network is also regularized in a few other ways. After each convolutional layer, an activation function is used to determine which neurons actually fire based on the results of the convolution. The activation function used is rectified linear units (ReLU), which sets the output to zero if the output of the convolution is negative, otherwise the original value is maintained. This helps deactivate unnecessary neurons in the network and reduce the computation cost of training and testing. Additionally, certain neurons are deactivated independently of ReLU in a process called dropout. A dropout rate of 2.5% is used after every max pooling or upconvolution operation. Finally, the outputs of each convolutional layer are normalized in a process called batch normalization, which improves the learning process for the neural network [38].

2.3.1 3-Fold Cross Validation & Accuracy Metrics

We train and test CNN models separately for the 6 groups of images: three different combinations of receivers (DAS alone, geophones alone, and the combination of the two) and the two sources (horizontal and vertical). To ensure accuracy metrics were not specific to one particular training and test split, cross-validation (CV) was performed using a three-fold CV. A 67/33 training-testing split was used: three sets of

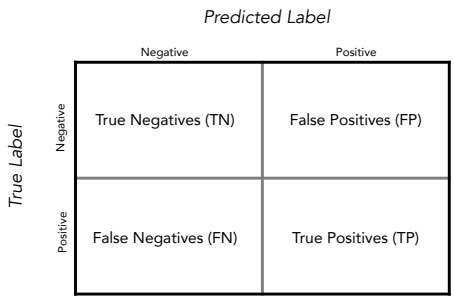

Figure 4: The confusion matrix contains all the accuracy metrics from the CNN. The rows contain the true labels; the columns the predicted labels. Accuracy, precision, recall and F1 metrics are all derived from the four entries in the matrix.

122 images for training and 61 for testing. The same three train/test split were used for all 6 source-receiver models to ensure consistency. The training and testing loss were monitored during the cross-validation. Training continued until the loss didn't improve after 5 epochs , where our chosen loss function is the dice coefficient [39]. Then the average of the 3 sets of evaluation metrics were used to compare the 6 source-receiver pairs, which will be discussed in the Results Section (Section 3.3).

Each sample originally consists of 150 by 155 pixels, but is resized to 250 by 250. Data augmentation performed via rotating the training images horizontally, vertically, and across the origin was examined but ultimately did not improve performance compared to using only the original RTM images. All six groups of images (geophone, DAS, and both for both sources) were standardized such that the mean of the data was zero and the standard deviation was equal to one.

Figure 4 depicts the standard confusion matrix for the binary case that is used to assess the accuracy of a classification algorithm. The rows hold the true class (e.g. not fault or fault), while the columns organize the resulting interpretations. Therefore, the quantities of correct classifications are along the diagonal, True Negatives (TN) and True Positives (TP), while the incorrect ones are on the off-diagonals: False Negatives (FN) and False Positives (FP). All of these quantities are used to calculate the metrics in Equations 4-7; as is usual, we compare the predicted class of the validated set, where the predictions are based on the models developed on the training samples.

$$accuracy = \frac{TN+TP}{TN+FP+TP+FN} \tag{4}$$

$$precision = \frac{TP}{TP+FP} \tag{5}$$

$$recall = \frac{TP}{TP+FN} \tag{6}$$

$$F_1 = \frac{2\ precision \cdot recall}{precision+recall} \tag{7}$$

$Accuracy$ (Eqn. 4), or bulk accuracy, is the percentage of correctly classified samples. $Precision$ (Eqn. 5) is the ratio of True Positives to all positive predictions, so it is normalized by all predictions of faults. In other words, of all the locations that were predicted to be faults, what fraction were actually faults? $Recall$ (Eqn. 6), on the other hand, is normalized by the true/actual class of faults: of all the locations that actually had faults, what fraction were correctly predicted as faults? In terms of Equation 1, $Recall$ is in the form of the likelihood ($Pr(\Theta^{int} = \theta_{j=fault,not\ fault}|\Theta = \theta_{fault})$) whereas $Precision$ is in the form of the

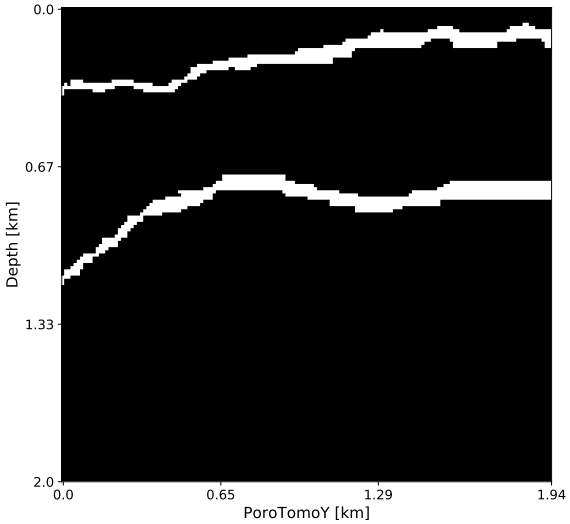

Figure 5: Faults located at j=20

posterior $Pr(\Theta = \theta_{i=faults,not\ faults}|\Theta^{int} = \theta_{faults})$, for the class of faults. F_1 is the harmonic mean of $Precision$ and $Recall$; harmonic means are often used to calculate the average of the ratios or rates. If either $Precision$ or $Recall$ is 0 or very low, then so is F_1.

In addition to the metrics in Equations 4 thru 7, we can calculate the Bayesian statistics, specifically the likelihoods,

$$Pr(\Theta^{int} = \theta_{fault}|\Theta = \theta_{fault})_{S,R} = \frac{TP}{TP+FN} \tag{8}$$

$$Pr(\Theta^{int} = \theta_{not\ fault}|\Theta = \theta_{fault})_{S,R} = \frac{FN}{TP+FN} \tag{9}$$

$$Pr(\Theta^{int} = \theta_{not\ fault}|\Theta = \theta_{not\ fault})_{S,R} = \frac{TN}{TN+FP} \tag{10}$$

$$Pr(\Theta^{int} = \theta_{fault}|\Theta = \theta_{not\ fault})_{S,R} = \frac{FP}{TN+FP} \tag{11}$$

for each of the six different trained CNN models ($S = vertical, horizontal$;$R = DAS, geophone, both$). The likelihoods indicate the ability of these sensors to record seismic signals that allow for the migration algorithms to delineate the faults from non-faults. These likelihoods can be transformed into the posterior (Eqn. 1) and used to calculate the value with imperfect information (Eqn. 2). From these comparisons, we can quantitatively compare single-component horizontal DAS and two-component geophones.

3 Results

In this section, we present and describe example images from slice j=20, shown in Figure 5, for both sources and for all three receivers. Next, we describe the average testing metrics for how well each CNN model performed given their training dataset over 3-fold cross validation. We will demonstrate which 2D slices had the lowest accuracy, i.e. had the highest training loss, for each source-receiver model. The testing metrics will include the posteriors (Eqn.1), which will ultimately be used to calculate a value with imperfect information (Eqn.2) for all 6 source-receiver combinations.

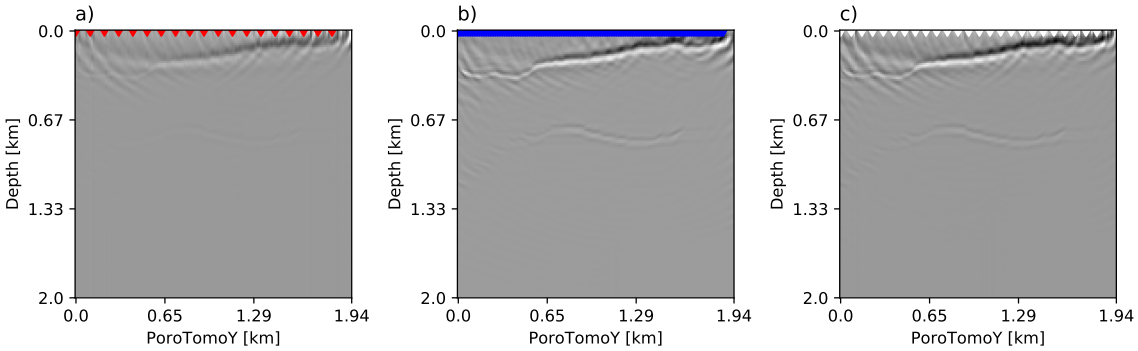

Figure 6: Migration images with vertical source : a) Geophones (locations in red), b) DAS (locations in blue), and c) Combined (sources in white).

3.1 Images from Vertical Force

Figure 6 contains the images produced from the elastic energy norm RTM using a vertical force with: a) sparsely sampled two-component geophones b) single-component DAS and c) a normalized and combined versions of a) and b). In Figure 6a spacing of geophones is represented by the red triangles; the deeper reflector is impossible to identify in the geophone image. The image is also covered with migration artifacts due to insufficient sampling of the wavefield. These artifacts are often called "migration smiles" for their shape; examples of these are present all along the PoroTomoY-axis at depths $\leq$0.5km in Figure 6a. The migration artifacts make it difficult for an interpreter and the CNN U-net to follow the shallow reflector.

Figure 6b is the image produced from the surface DAS fiber (a virtual horizontal-component receiver every one meter, shown in blue). The shallow reflector in this image is sharp and continuous, allowing for easy interpretation. Although migration artifacts are still present along the PoroTomoY-axis, there are artifacts that are different from those shown in Figure 6a. These migration artifacts are now due to fake modes present because the wavefield is extrapolated using only the x-component data that was recorded with DAS fiber. These fake modes are a specific type of artifact that results from a deficient extrapolation of the receiver wavefield; this is expected, given that seismic force is excited vertically. If the faults were largely horizontal, given the relative short offset, the majority of the reflected energy would arrive perpendicular to the DAS fiber, not along the fiber which is its direction of highest sensitivity. However, as seen in Figure 2, the faults have a variety of dips, including very steeply dipping. By simulating the full wavefield (e.g. not ray-based), there may be significant reflections that do not arrive broadside to the horizontal fiber. In our noise-free simulations, these signals are significant, which may not be the case with land-based DAS field data.

The images in Figures 6a and Figure 6b contain two different migration artifacts: migration smiles and fake modes. Stacking the images could reduce the noise and highlight the reflection events. The amplitudes of both images are normalized by the maximum and then stacked to produce Figure 6c. Although the reflectors are slightly enhanced compared to the DAS image, Figure 6c unfortunately, still has many artifacts in it. As described earlier, the authors acknowledge that this is not the ideal way to combine the two images from the different sensors. We propose other options in the Discussion section.

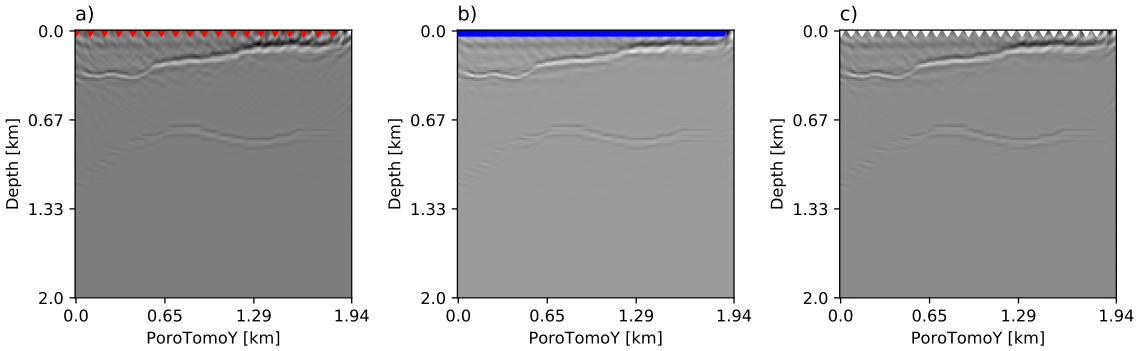

Figure 7: Migration images with horizontal source : a) Geophones (locations in red), b) DAS (locations in blue), and c) Combined (sources in white).

3.2 Images from Horizontal Force

Different source types can generate different polarizations of reflection events. For this reason, the second 2D experiment uses the same geometries and models as the first experiment, but now a horizontal force is used to generate data. The image produced from elastic energy norm RTM with sparsely sampled two-component geophones and a horizontal force is shown in Figure 7a. This image still contains migration artifacts, but compared to Figure 6a, the reflector is much easier to follow. The receiver sampling was not changed, so the image still contains migration artifacts due to insufficient sampling of the wavefield. However, compared to the vertical source experiment (Figure 6a), the deeper reflector is now easier to identify in Figure 7a. A potential explanation for this improvement is that the horizontal source produces more of the slower S-waves which have smaller wavelengths (versus P-waves) providing a better resolution of reflectors.

The image produced from elastic energy norm RTM with DAS data and an horizontal-source is shown in Figure 7b. Compared to Figure 6b, the migration artifacts have diminished. The deeper reflector is easier to observe and interpret , which suggests that a horizontal force is more beneficial for near-offset DAS surveys. As described in Section 2.2, short-offset P-wave reflections will not be recorded on surface DAS at normal incidence, so the S-wave source may provide more variety of incidence angle from the deeper reflector. Again keeping in mind that the elastic RTM models the full wavefield, and in these synthetic cases, no noise impedances the re-construction of deeper and weaker signals. The DAS data are sampling the reflected wavefields well.

The images are normalized and stacked just as it was done for the previous example. The results are shown in Figure 7c. Figure 7c shows both reflectors clearer than Figure 6c.

3.3 Reliability & $V_{imperfect}$ measures from CNN Analyses

Now that spatial models from geophone, DAS and both sensor data are produced, the next step is to obtain statistics that describe how well fault and non-faults could be interpreted from these images. The true fault model from Ref. [22] is used as labels for the RTM models, and ultimately to train the U-net to determine whether each pixel in the model is fault or not-fault.

Due to the class imbalance (much higher occurrence of non-fault labels versus fault labels), accuracy did not differentiate strongly between the models. All trained models achieved over 99% accuracy, but so would

Table 1: **Vertical Source**: metrics for each receiver type

Metric	DAS	Geophone	Combined
Average F1-score	0.919	0.877	0.907
Average Accuracy	0.996	0.994	0.995
Average Precision	0.931	0.916	0.925
Average Recall	0.906	0.842	0.890
Average Loss	0.003	0.004	0.003

Table 2: **Horizontal Source**: metrics for each receiver type

Metric	DAS	Geophone	Combined
Average F1-score	0.939	0.931	0.930
Average Accuracy	0.997	0.996	0.996
Average Precision	0.952	0.946	0.952
Average Recall	0.926	0.916	0.910
Average Loss	0.002	0.002	0.002

a model that predicted non-fault across all slices. F_1-score, again the harmonic mean of $Precision$ and $Recall$, can highlight the difference between these models. The reported metrics were averaged over each 3-folds of cross validation. All models were run for at least 150 epochs, after which, the stopping criteria was for when the training loss didn't improve after 10 epochs *and* the testing loss didn't improve after 5 epochs.

Table 1 contains the metrics for the vertical-source data. DAS performed best (F_1=0.919), followed by the combined data set (F_1=0.907). Geophone trailed behind both (F_1=0.877). This suggests that the geophone image ultimately reduces the accuracy of the DAS image when the two images are combined. Also note that the geophone trained model had the highest testing loss. Therefore, the quality of geophone images with the vertical source resulted in a higher loss compared to the DAS. $Recall$ is the likelihood for the positive case; for our example, it is the likelihood for $\theta = fault$ (Equation 6). The best-to-worst order for the $Recall$ statistic for the vertical source is the same order as in the F_1 score: DAS, both and geophone.

Table 2 summarizes the average metrics for the horizontal-source data, where now the order of largest to smallest F_1 score is DAS (0.939), geophones (0.931) and both (0.930). Compared to the vertical source, the geophone-trained CNN is closer to the DAS-trained CNN: the $F_{1\ geophone}$ score is 99% of the $F_{1\ DAS}$ compared to 95% in the vertical case. $Recall$ is in the same order as the F_1, with the geophone-trained CNN model having much better $Recall$ than the CNN trained on images combing both receivers. Overall, models trained with horizontal-source data perform better than models trained with vertical-source data, indicating that the horizontal data better indicate where faults are located in the subsurface.

It is important to consider the posteriors (Equation 1), as they indicate the frequency at which any of the four situations in the confusion matrix (Figure 4) can occur. Neither F_1 nor $Recall$ consider the rate at which true negatives occur, and that turns out to differentiate the six CNN models trained on the different images. A posterior reliability of information can be calculated with the results from the testing data (Equations 1 and 8- 11). The posterior probabilities from the six CNN models the resulting $V_{imperfect}$ are shown in Figures 8 and 9 for the vertical and horizontal source, respectively. Consistent with their F_1, $Recall$ and their true negative posterior value, for the vertical case, DAS, both and geophone have the most to least

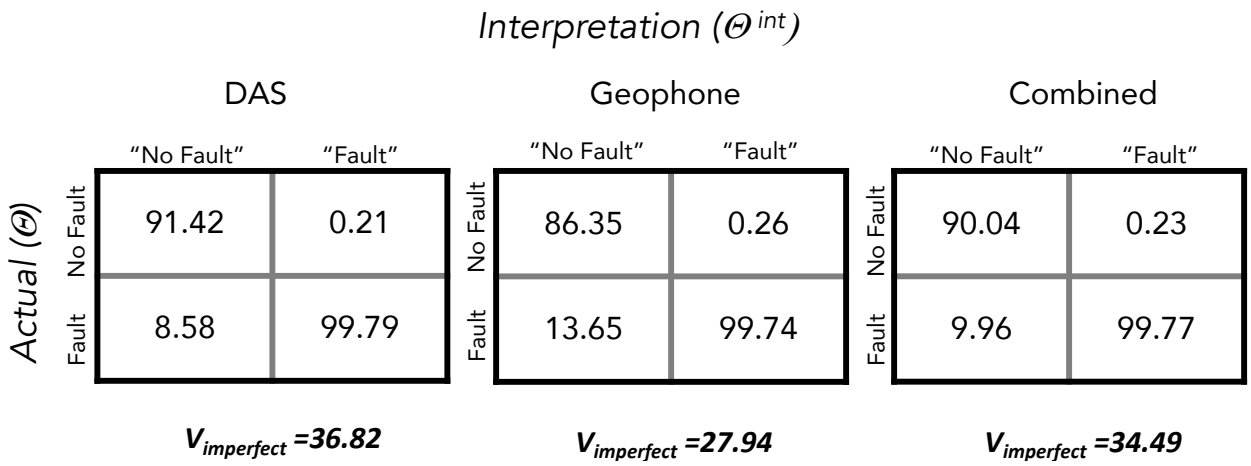

Figure 8: Posteriors & $V_{imperfect}$ calculated from 3 U-net CNN's using Vertical Source Images

Table 3: Nominal $v_a(\Theta)$

	Θ=No Fault	**Θ=Fault**
a=No action	0	-100
a=Action (e.g. drill)	-375	100

$V_{imperfect}$. For the horizontal case, DAS, geophone and both are the order from most to least $V_{imperfect}$, also consistent with the rate of true negatives, F_1, and $Recall$ for those CNN models.

As seen in Equation 2, certain values must be defined to calculate $V_{imperfect}$. For demonstration purposes, we assume a prior of 50%/50% for fault/no fault. Additionally, the two decision actions are deemed to drill or do nothing. Table 3 contains the nominal value outcomes for all possible actions and subsurface scenarios (fault/no fault). When one drills near a fault (a proxy for permeability), $v_{a=drill}(\theta = fault)$=\$100, whereas if it is a dry hole $v_{a=drill}(\theta = no\ fault)$=\$-375. When not drilling and no fault, $v_{a=nothing}(\Theta = no\ fault)$=\$0, while with a fault, we model this lost opportunity with $v_{a=nothing}(\Theta = no\ fault)$=-\$100.

3.3.1 Training Loss Evaluation

This section evaluates which 2D fault cross sections performed the worst, thus reducing the accuracy of the model, and ideally, giving insight into the physics of each source-receiver combination. For this we omit evaluating combined (DAS + geophone) images. Figure 10 contains the training loss value for each 2D cross sections for the four CNN models trained with both sources and DAS and geophone. All training losses are the highest on the right side of the plot, which are cross sections on the south side of the PoroTomo grid. An example of the fault locations and dips for this area is shown in Figure 2, and the six corresponding migration image examples are seen in Figure 3. The fault's location and its changing dip (on the rightside in Figure 2) do not provide adequate reflection energy to neither the geophones nor DAS.

Figure 10 also highlights the 2D cross sections, outside of the southern area, that have the highest loss for each of the four models. The highest loss among this subgroup belongs to the vertical source with geophones (red downward-pointing triangle), which is at index=105. The migration images and the true fault labels are shown in 10. As seen in the fault labels, the fault locations and dips are nearly identical for these two

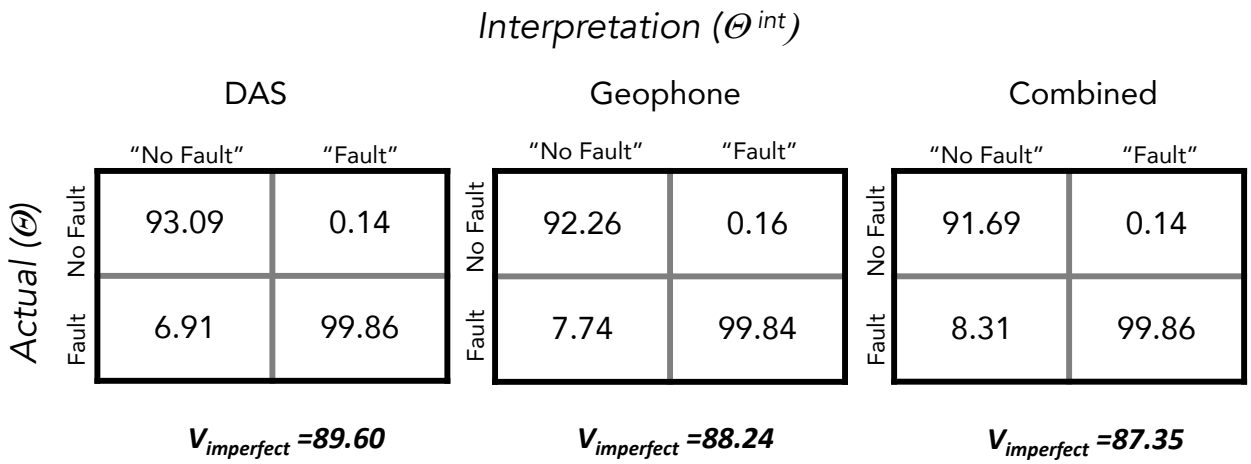

Figure 9: Posteriors & $V_{imperfect}$ calculated from 3 U-net CNN's using Horizontal Source Images

locations (index values 92 and 105). The deeper fault is slightly longer than the shallow fault. Therefore, when the source-receiver combination does not predict well the location of the deep fault, this results in a higher loss. In this case, the horizontal source combined with the high spatial density of DAS does the best job (cyan right-pointing triangle).

4 Discussion

Our main intent for utilizing the CNN is to obtain less subjective and computationally efficient statistics from seismic migration models. Six CNN's were trained separately on migration images from two sources and three receiver groups: geophone, DAS and combination experiments. By using migration images that simulate what is measured by the horizontal-component, 1-meter-spaced DAS and the two-component, sparse geophones, we have attempted to achieve realistic and useful reliability estimations of each. However, our methodology does have limitations that can affect the accuracy of its $V_{imperfect}$ calculations.

Field data will have challenges which were not included in our synthetic modelling. They will lead to larger errors and be more detrimental to DAS than geophones. Ground-roll and near-surface statics (heterogeneities) would overwhelm a weak DAS signal in many cases. DAS interrogators, which are responsible for sensing the distributed strain along the fiber, are noisier than geophone recording systems. Additionally, velocity model uncertainties are always an issue with migration approaches. For elastic migrations, knowledge of the S-wave velocity is imperative. Unfortunately, there is higher uncertainty in S-wave velocity which would introduce more errors into the migration results.

As mentioned in the Methodology section, our representation of combining DAS and two-component geophone is imperfect. We normalize the RTM images from geophones and DAS and adding them together. Ideally, numerical modeling codes would be available that allow for the simultaneous imaging of displacement and stress (strain). A potential improvement over our approach is to avoid combining the two images altogether. Instead, one could provide both images as features to train a CNN with both images (geophone and DAS). The testing validation from this type of CNN could represent added value of DAS versus geophones alone.

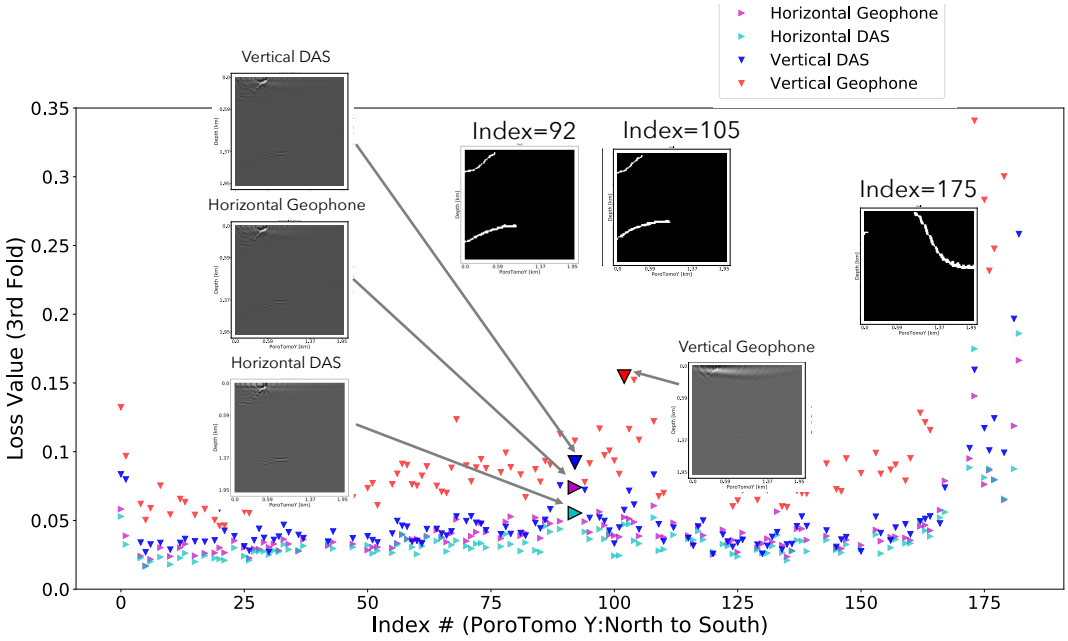

Figure 10: Training Loss for each of the four source and receiver combinations.

Figure 10 shows the training loss curves for four of the different CNN models. Each point shows the loss for each profile (cross section). The middle cross sections and the southern cross sections do the poorest: the deeper and the end of the dipping fault are not properly imaged. This is due to insufficient aperture in the migration. One technique used in migration is compensation by source illumination, which helps where source wavefield is weak. This could have improved images, and maybe changed our reliability measures for the six source-receiver groups.

One of the main road-blocks to calculating VOI on geophysical models, especially seismic, is the computational time to obtain one model, and the added computation of estimating accuracy statistics. Therefore, it is of the upmost importance to have computationally efficient VOI methodologies, to start assess the value of information from different sensors. This is the main motivator to use the accuracy statistics from CNN's trained on images from the different sensors. Typically, CNN models are trained and tested with the objective of developing a model that can predict the labels. Our unconventional use of CNN's could provide overly optimistic reliability measures compared to what an actual interpreter could decipher from a seismic image. Although our approach to the training and testing of the CNN model's was identical for both geophone, DAS and the combination of the two, it is possible that our stopping criteria (5 epochs without testing loss improvement) could have influenced the results of the scenarios presented in this paper. However, the goal was to develop an efficient methodology that includes spatial seismic models.

Other sources of over-optimistic posterior measurements could be due to 1) not including the coupling challenges of DAS and 2) not modeling in 3D. How effectively the energy of seismic waves will be recorded by DAS depends on how well-coupled the fiber is the subsurface media. Currently, the codes available do not include modeling capability to adjust coupling. Poor coupling will affect the fiber's ability to record signal that can be reconstructed into images of fault reflections. 3D modeling would more accurately test the full

DAS fiber directionality.

This paper is the first demonstration of assessing the value of seismic data by assessing the migration models accuracy. We have used the PoroTomo field acquisition for our experiments, but our methodology is useful beyond this singular example. We believe this methodology may have increasing importance, as permanent horizontal DAS measurements could become pervasive as the technology improves. Telecommunications fibers have been proven to be capable of serving as urban sensors that can reliably define the shear-wave velocity of the near-surface for kilometer-long transects [40].

5 Conclusions

Value of information (VOI) provides a quantitative and agnostic metric for the utility of interpretations from different sensors. Although VOI has historically been used in oil and gas as a decision tool for data collection, its application has been limited to non-dimensional data (e.g. no spatial context) or oversimplified models from geophysical observations. This paper presents several innovations to previous VOI methodologies that 1) include the spatial structure provided by active-source seismic methods and 2) improve computational efficiency in obtaining accuracy statistics of seismic images/models by utilizing convolutional neural networks. We believe this methodology may have increasing importance, to evaluate acquisition geometries for any kind of sensor.

In the case of horizontal DAS, we modeled the insensitivity of DAS to broadside energy (e.g. seismic signals that arrive perpendicular to the DAS cable) and how it affects the ability to image subsurface structures or properties that will subsequently affect drilling or exploration decisions. Geophone spacing in the PoroTomo survey was too sparsely arranged, and the hypothesis is that DAS, which samples the Earth's response at a higher spatially density, could improve images generated by sparse geophones. This hypothesis was tested in 2D using elastic numerical modeling and elastic RTM. Both 2D experiments (vertical and horizontal forces) concluded that DAS was marginally more successful at locating fault positions in 2D. The confusion matrix from the CNN model trained on images utilizing both sensors' data quantitatively confirmed that true positives and negatives are increased when comparing confusion matrices from sparse 2C geophones alone.

We do not conclude that universally DAS will always add value to sparse geophones. However our methodology can provide guidance on which scenarios the high spatial density overcomes the broadside sensitivity of DAS. Ideally, the field data will be assessed in the future with more expertise and resources in land-data processing. The idea of using both data types in simultaneous imaging should also be explored to produce more detailed images. Future work should include coupling effects for a more realistic representation of what DAS can measure in the field. Imaging these faults in detail can provide information on driving factor behind the recharge of a geothermal reservoir.

Acknowledgments

The work presented herein was funded in part by the Office of Energy Efficiency and Renewable Energy (EERE), U.S. Department of Energy, under Award Number DE-EE0006760. We thank the anonymous reviewer whose meticulous work greatly improved the manuscript's clarity.

List of Tables

Table 1: Vertical Source: metrics for each receiver type
Table 2: Horizontal Source: metrics for each receiver type
Table 3: Nominal decision outcome values: $v_a(\Theta)$

List of Figures

Figure 1: PoroTomo survey geometry. Green dots represent source locations, red dots represent geophone locations, and the blue line represents the surface DAS layout.

Figure 2: a) (Siler and Faulds, 2013) a priori fault model with source locations in green on the surface. b) One example 2D cross section from the 3D model in a, represented by 150x155 pixels. The faults (in white) serve as reflectivity boundary for seismic exploration.

Figure 3: Workflow for 2D fault images and their respective statistics. Section 2.1 Fault model: the decision parameter = seismic reflectors = labels in machine learning. Section 2.2 Seismic images: imperfect information about the fault locations (2D "features"). Rows= sources type. Columns= receiver type. Section 2.3: Posterior statistics from CNN.

Figure 4: The confusion matrix contains all the accuracy metrics from the CNN. The rows contain the true labels; the columns the predicted labels. Accuracy, precision, recall and F1 metrics are all derived from the four entries in the matrix.

Figure 5: Faults located at j=20

Figure 6: Migration images with vertical source : a) Geophones (locations in red), b) DAS (locations in blue), and c) Combined (sources in white).

Figure 7: Migration images with horizontal source : a) Geophones (locations in red), b) DAS (locations in blue), and c) Combined (sources in white).

Figure 8: Posteriors & Vimperfect calculated from 3 U-net CNN's using Vertical Source Images

Figure 9: Posteriors & Vimperfect calculated from 3 U-net CNN's using Horizontal Source Images

Figure 10: Training Loss for each of the four source and receiver combinations.

References

[1] Howard, R. a., 1966, "Information Value Theory," Systems Science and Cybernetics, IEEE Transactions on, **2**(1), pp. 22–26.

[2] Houck, R. T., 2004, "Predicting the economic impact of acquisition artifacts and noise," The Leading Edge, **23**(1), pp. 33–36.

[3] Houck, R. T., 2007, "Time-lapse seismic repeatability ? How much is enough?" The Leading Edge, pp. 828–834.

[4] Eidsvik, J., Bhattacharjya, D., and Mukerji, T., 2008, "Value of information of seismic amplitude and CSEM resistivity," Geophysics, **73**(4), p. R59.

[5] Bratvold, R. B., Bickel, J. E., Risk, A., and Lohne, H. P., 2009, "Value of Information in the Oil and Gas Industry : Past, Present, and Future," Society of Peteroleum Engineers:Reservoir Evaluation & Engineering, **12**(August 2009), pp. 630–638.

[6] Trainor-Guitton, W. J., Caers, J. K., and Mukerji, T., 2011, "A Methodology for Establishing a Data Reliability Measure for Value of Spatial Information Problems," Mathematical Geosciences, **43**(8), pp. 929–949.

[7] Trainor-Guitton, W. J., 2014, "A geophysical perspective of value of information: Examples of spatial decisions for groundwater sustainability," Environment Systems and Decisions, **34**(1), pp. 124–133.

[8] Nenna, V. and Knight, R., 2014, "Demonstration of a value of information metric to assess the use of geophysical data for a groundwater application," Geophysics, **79**(1).

[9] Trainor-Guitton, W. J., Hoversten, G. M., Ramirez, A., Roberts, J., Juliusson, E., Key, K., and Mellors, R., 2014, "The value of spatial information for determining well placement : A geothermal example," Geophysics, **79**(5), pp. W27–W41.

[10] Trainor-Guitton, W. J., Hoversten, G. M., Nordquist, G., and Intani, R., 2017, "Value of MT inversions for geothermal exploration : accounting for multiple interpretations of field data & determining new drilling locations," Geothermics, **66**(66), pp. 13–22.

[11] Feigl, K. L., Lancelle, C., Lim, D. D., Parker, L., Reinisch, E. C., Ali, S. T., Fratta, D., Thurber, C. H., Wang, H. F., Robertson, M., Coleman, T., Miller, D. E., Lopeman, J., Spielman, P., Akerley, J., Kreemer, C., Morency, C., and Matzel, E., 2018, "Overview and Preliminary Results from the Poro-Tomo Project at Brady Hot Springs, Nevada: Poroelastic Tomography by Adjoint Inverse Modeling of Data from Seismology, Geodesy, and Hydrology," *Stanford Geothermal Workshop*.

[12] Cardiff, M., Lim, D. D., Patterson, J. R., Akerley, J., Spielman, P., Lopeman, J., Walsh, P., Singh, A., Foxall, W., Wang, H. F., et al., 2018, "Geothermal production and reduced seismicity: Correlation and proposed mechanism," Earth and Planetary Science Letters, **482**, pp. 470–477.

[13] Queen, J. H., Daley, T. M., Majer, E. L., Nihei, K. T., Siler, D. L., and Faulds, J. E., 2016, "Surface Reflection Seismic and Vertical Seismic Profile at Brady ' s Hot Springs , NV , USA," *Stanford Geothermal Workshop*, pp. SGP–TR–209.

[14] Trainor-Guitton, W., Guitton, A., Jreij, S., Powers, H., and Sullivan, B., 2019, "3D Imaging of Geothermal Faults from a Vertical DAS Fiber at Brady Hot Spring, NV USA," Energies, **12**(7), p. 1401.

[15] Claerbout, J., 1971, "Toward a unified theory of reflector mapping," Geophysics, **36**(June), pp. 467–481.

[16] Feigl, K. L., Lancelle, C., Lim, D. D., Parker, L., Reinisch, E. C., Ali, S. T., Fratta, D., Thurber, C. H., Wang, H. F., Robertson, M., Coleman, T., Miller, D. E., Lopeman, J., Spielman, P., Akerley, J., Kreemer, C., Morency, C., and Matzel, E., 2017, "Overview and Preliminary Results from the Poro-Tomo Project at Brady Hot Springs, Nevada: Poroelastic Tomography by Adjoint Inverse Modeling of Data from Seismology, Geodesy, and Hydrology," *Stanford Geothermal Workshop*.

[17] Szegedy, C., Vanhoucke, V., Ioffe, S., Shlens, J., and Wojna, Z., 2015, "Rethinking the Inception Architecture for Computer Vision," .

[18] Ronneberger, O., Fischer, P., and Brox, T., 2015, "U-Net: Convolutional Networks for Biomedical Image Segmentation," arXiv:1505.04597 [cs], arXiv: 1505.04597.

[19] Wang, H. F., Zeng, X., Miller, D. E., Fratta, D., Feigl, K. L., Thurber, C. H., and Mellors, R. J., 2018, "Ground motion response to an ML 4.3 earthquake using co-located distributed acoustic sensing and seismometer arrays," Geophysical Journal International, **213**(3), pp. 2020–2036.

[20] Li, Z. and Zhan, Z., 2018, "Pushing the limit of earthquake detection with distributed acoustic sensing and template matching: a case study at the Brady geothermal field," Geophysical Journal International, **215**(3), pp. 1583–1593.

[21] Folsom, M., Lopeman, J., Perkin, D., and Sophy, M., 2018, "Imaging Shallow Outflow Alteration to Locate Productive Faults in Ormat ' s Brady ' s and Desert Peak Fields Using CSAMT," *Stanford Geothermal Workshop*, pp. 1–11.

[22] Siler, D. L. and Faulds, J. E., 2013, "Three-dimensional geothermal fairway mapping: Examples from the Western Great Basin, USA,," GRC Transactions, **7**, pp. 327–332.

[23] Dean, T., Cuny, T., and Hartog, A. H., 2017, "The effect of gauge length on axially incident P-waves measured using fibre optic distributed vibration sensing," Geophysical Prospecting, **65**(1), pp. 184–193.

[24] Lim Chen Ning, I. and Sava, P., 2018, "Multicomponent distributed acoustic sensing: Concept and theory," Geophysics, **83**(2), pp. P1–P8.

[25] Fomel, S., Sava, P., Vlad, I., Liu, Y., and Bashkardin, V., 2013, "Madagascar: Open-source software project for multidimensional data analysis and reproducible computational experiments," Journal of Open Research Software, **1**(1).

[26] Rocha, D., Tanushev, N., and Sava, P., 2016, "Isotropic elastic wavefield imaging using the energy norm," Geophysics, **81**(4), pp. S207–S219.

[27] Lumens, P., 2014, "Fibre-optic sensing for application in oil and gas wells," Ph.D. thesis, Eindhoven University of Technology, doi:10.6100/IR769555, `http://alexandria.tue.nl/extra2/769555.pdf{%}5Cnhttp://repository.tue.nl/769555`

[28] Krohn, D. A., MacDougall, T., and Mendez, A., 2000, *Fiber optic sensors: fundamentals and applications*, Isa.

[29] Mestayer, J., Cox, B., Wills, P., Kiyashchenko, D., Lopez, J., Costello, M., Bourne, S., Ugueto, G., Lupton, R., Solano, G., et al., 2011, "Field trials of distributed acoustic sensing for geophysical monitoring," *SEG Technical Program Expanded Abstracts 2011*, Society of Exploration Geophysicists, pp. 4253–4257.

[30] Barberan, C., Allanic, C., Avila, D., Hy-Billiot, J., Hartog, A., Frignet, B., and Lees, G., 2012, "Multi-offset seismic acquisition using optical fiber behind tubing," *74th EAGE Conference and Exhibition incorporating EUROPEC 2012*.

[31] Cox, B., Wills, P., Kiyashchenko, D., Mestayer, J., Lopez, J., Bourne, S., Lupton, R., Solano, G., Henderson, N., Hill, D., et al., 2012, "Distributed acoustic sensing for geophysical measurement, monitoring and verification," CSEG Recorder, **37**(02), pp. 7–13.

[32] Daley, T. M., Freifeld, B. M., Ajo-Franklin, J., Dou, S., Pevzner, R., Shulakova, V., Kashikar, S., Miller, D. E., Goetz, J., Henninges, J., et al., 2013, "Field testing of fiber-optic distributed acoustic sensing (DAS) for subsurface seismic monitoring," The Leading Edge, **32**(6), pp. 699–706.

[33] Mateeva, A., Lopez, J., Potters, H., Mestayer, J., Cox, B., Kiyashchenko, D., Wills, P., Grandi, S., Hornman, K., Kuvshinov, B., et al., 2014, "Distributed acoustic sensing for reservoir monitoring with vertical seismic profiling," Geophysical Prospecting, **62**(4), pp. 679–692.

[34] Hornman, J., 2017, "Field trial of seismic recording using distributed acoustic sensing with broadside sensitive fibre-optic cables," Geophysical Prospecting, **65**(1), pp. 35–46.

[35] Yang, T., Shragge, J., and Sava, P., 2013, "Illumination compensation for image-domain wavefield tomography," Geophysics, **78**(5), pp. U65–U76.

[36] Matzel, E. M., Zeng, X., Thurber, C., and Morency, C., 2017, "Using Virtual Earthquakes to Characterize the Material Properties of the Brady Hot Springs , Nevada," Geothermal Resources Council.

[37] Long, J., Shelhamer, E., and Darrell, T., 2015, "Fully Convolutional Networks for Semantic Segmentation," *Proceedings of the IEEE conference on computer vision and pattern recognition*, Vol. 2015, pp. 3431–3440, doi:10.1109/IJCNN.2017.7966367.

[38] Ioffe, S. and Szegedy, C., 2015, "Batch Normalization: Accelerating Deep Network Training by Reducing Internal Covariate Shift," CoRR, **abs/1502.03167**.

[39] Milletari, F., Navab, N., and Ahmadi, S.-A., 2016, "V-Net: Fully Convolutional Neural Networks for Volumetric Medical Image Segmentation," pp. 565–571, doi:10.1109/3DV.2016.79.

[40] Jousset, P., Reinsch, T., Ryberg, T., Blanck, H., Clarke, A., Aghayev, R., Hersir, G. P., Henninges, J., Weber, M., and Krawczyk, C. M., 2018, "Dynamic strain determination using fibre-optic cables allows imaging of seismological and structural features," Nature Communications, **9**(1), p. 2509.